Electronic Supplementary Material (ESI) for Catalysis Science & Technology.

Electronic Supporting Information – Structural dynamics in Ni-Fe catalysts during CO_2 methanation – role of iron oxide clusters

Marc-André Serrer,[a,b] Abhijeet Gaur[a,b], Jelena Jelic[b], Sebastian Weber[a,b], Charlotte Fritsch[a,b], Adam H. Clark[c], Erisa Saraçi[a,b], Felix Studt[b], Jan-Dierk Grunwaldt[a,b]*

[a]Institute for Chemical Technology and Polymer Chemistry, Karlsruhe Institute of Technology (KIT), 76131 Karlsruhe, Germany

[b]Institute of Catalysis Research and Technology, Karlsruhe Institute of Technology (KIT), 76344 Eggenstein-Leopoldshafen, Germany

[c]SuperXAS beamline, Paul Scherrer Institut (PSI), 5232 Villigen, Switzerland

1 Table of Content

1 Table of Content 1

2 Experimental 2

2.1 Experimental setup for operando synchrotron studies 2

2.2 Rietveld refinement of synchrotron-based powder XRD 2

3 Additional results 3

3.1 Catalyst activation and Ni_3Fe alloy formation 3

3.2 Active state of the Ni-Fe catalyst under steady state conditions 4

3.2.1 EXAFS fitting details 5

3.2.2 Rietveld refinement of synchrotron-based powder XRD 9

3.3 Development of a structural model 16

3.4 Catalyst response to periodic CO_2 feed modulations (MES) 17

3.4.1 Steady state of Ni/Al_2O_3 and $Ni\text{-}Fe/Al_2O_3$ before and after the MES experiment 17

3.4.2 Ni K-edge XANES spectra of Ni/Al_2O_3 and $Ni\text{-}Fe/Al_2O_3$ before the MES experiment 18

3.4.3 Fe K-edge XANES spectra of Ni/Al_2O_3 and $Ni\text{-}Fe/Al_2O_3$ before the MES experiment 19

3.4.5 Time-resolved XANES spectra of the monometallic Ni/Al_2O_3 catalyst 20

3.4.6 Time-resolved XANES spectra of the bimetallic $Ni\text{-}Fe/Al_2O_3$ catalyst 21

3.4.7 Phase-resolved Ni K-edge MES spectra of Ni/Al_2O_3 and $Ni\text{-}Fe/Al_2O_3$ catalyst 22

3.5 Calculations on the stability of the Ni-Fe alloy and formation of FeO_x clusters 25

3.5.1 Defining U value for GGA+U method 25

3.5.2 Oxygen adsorption on $Ni_4Fe(111)$ alloy 25

3.5.3 $(FeO)x/Ni_4Fe(111)$* surface model 27

3.5.4 Phase diagram 28

3.5.5 Oxygen hydrogenation 30

3.5.5 Ni vs Ni_4Fe vs $(FeO)_6/Ni4Fe$* 30

4 References 32

2 Experimental

2.1 Experimental setup for operando synchrotron studies

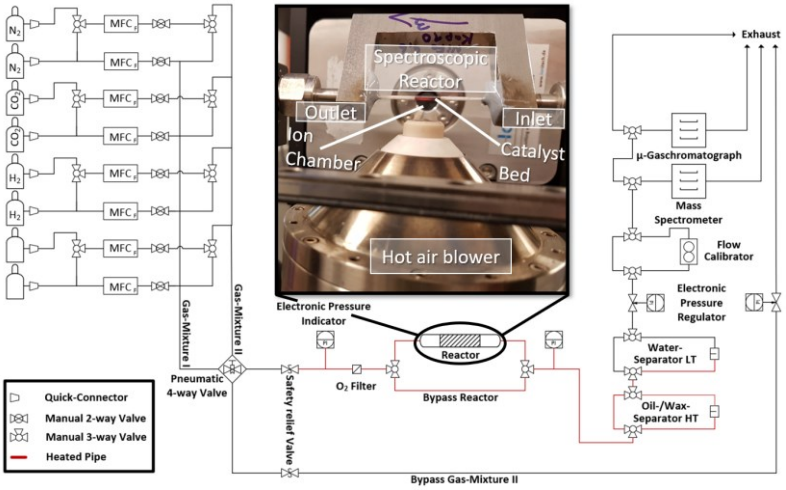

Figure S 1: *Operando* setup used for the combined XAS & XRD measurements, as well as the MES experiments presented in this study.

2.2 Rietveld refinement of synchrotron-based powder XRD

FullProf software package was used for refinement of PXRD data.[1] An instrumental resolution file was first obtained by profile fitting of a LaB_6 NIST 640b standard to correct for peak broadening based on the instrument. The nano-crystalline nature of the used γ-Al_2O_3 makes it difficult to refine this phase well, which can be especially seen in deviations of the measured and calculated patterns at 17.5 ° or 20.5 ° in all refinements shown in Figure S 11 - Figure S 15. However, reflections for Ni phase and overlapping reflections between both phases can be described well. Thermal displacement parameters and occupancies could not be stably refined and were fixed to meaningful or initial values from the structural models. The obtained fractions for both phases are shown in Figure S 8 and listed in Table S 2 - Table S 7 while the error for the γ-Al_2O_3 phase is quite high. Additionally, the values do not match the expected ones of 17 wt.% for $Ni_{3.0}Fe$ and 83 wt.% for γ-Al_2O_3 or as determined by elemental analysis. Reasons for this are that we are only considering the metal to be Ni and not the contribution of Fe, the γ-Al_2O_3 phase is not described well potentially overestimating the amount of γ-Al_2O_3 and only crystalline parts of the metal nanoparticles account to the phase fraction. Therefore, the obtained fractions should be rather considered qualitatively and not quantitatively.

2.3 Calculation of alloy composition using Vegard´s law

The calculation of the alloy composition was performed using Vegard´s law[2], *i.e.* the linear correlation of the lattice parameter a to the respective fraction of Ni (fcc, a=3.520 Å) and Ni_3Fe (fcc, a=3.553 Å)[3-9]. The lattice parameter of the alloy was determined based on the shifted Ni reflections obtained in the refined XRD results (cf. sections 2.2 and 3.2.2).

3 Additional results

3.1 Catalyst activation and Ni_3Fe alloy formation

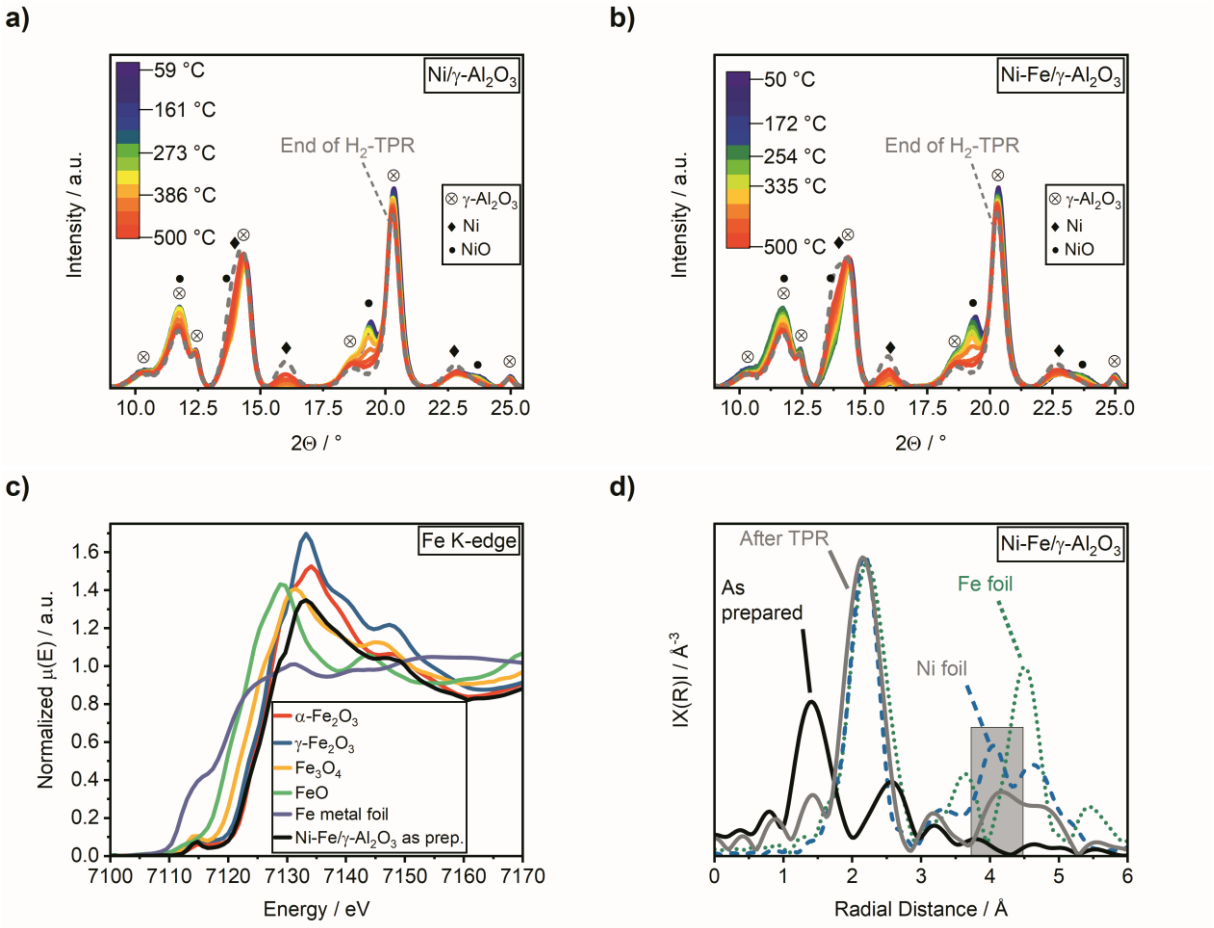

Figure S 2: Continuously recorded XRD data of (a) Ni/γ-Al_2O_3 and (b) Ni-Fe/γ-Al_2O_3 during H_2-TPR at 6 bar. (c) Fe K-edge XANES spectra of the Ni-Fe/γ-Al_2O_3 catalyst as prepared in comparison to references and (d)k^2-weighted FT-transformed EXAFS spectra obtained at the Fe K-edge of the Ni-Fe/γ-Al_2O_3 catalyst before and after H_2-TPR in comparison to a Ni and Fe metal foil.

3.2 Active state of the Ni-Fe catalyst under steady state conditions

To verify the formation of FeO_x, the Fe K-edge XANES spectra were compared to their state during H_2-TPR (Figure S 3).

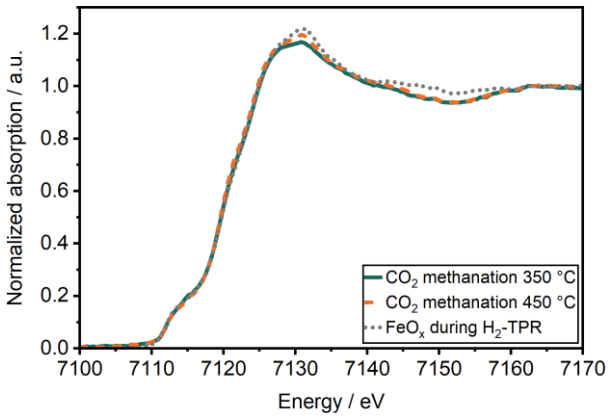

Figure S 3: Normalized XANES spectra at the Fe K-edge of the Ni-Fe/Al_2O_3 catalyst during methanation of CO_2 compared to the partially oxidized spectra during H_2-TPR.

A good comparability between the state of iron during CO_2 methanation (Figure S 3, green and orange dotted line) to the state during H_2-TPR (grey dotted line) was given. In case of carbide formation, a different shape of the pre-edge feature would be expected.[10] Hence, it can be concluded that FeO_x is formed.

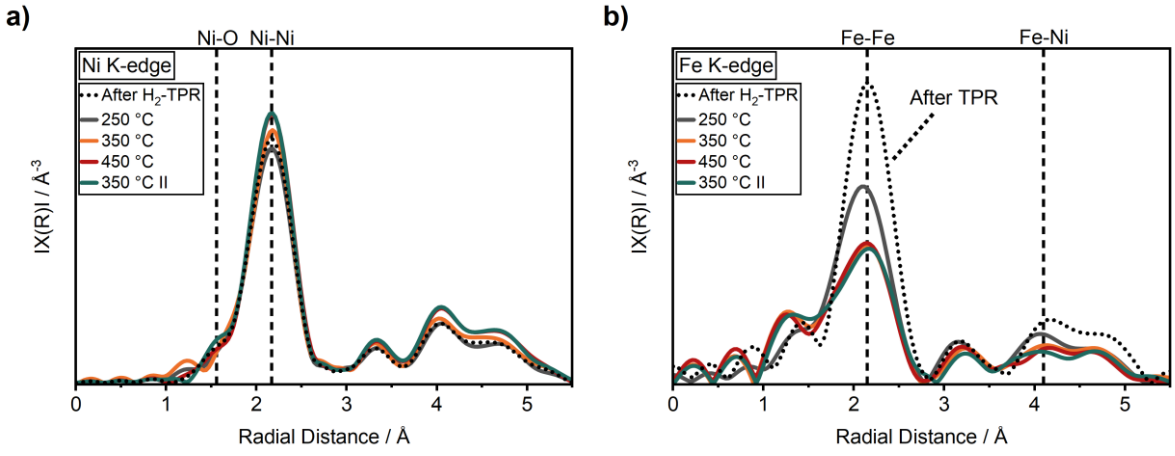

Figure S 4: k^2-weighted Fourier transformed EXAFS of the Ni (a) and Fe (b) K-edge spectra of the 17 wt.% Ni_3Fe/γ-Al_2O_3 catalyst at 50 °C after applying methanation conditions of 20 ml/min 50 vol% H_2:CO_2=4:1 in N_2 at atm and various temperatures for 1 h.

Temperature effects can be excluded in this FT-EXAFS data, as all spectra were recorded at 50 °C after the respective temperature step. The coordination number of Ni decreased slightly after switching to methanation conditions at 250 °C from 8.2 ± 1.2 to 8.0 ± 1.2 accompanied by decrease in the

coordination number of Fe from 6.1 ± 1.2 to 4.4 ± 1.1. Furthermore, the Fe-Ni backscattering peak at 4 Å declined. The decreased Fe-Fe coordination might either be due to FeO formation or due to segregation of Fe to the surface of the alloyed particles. Due to insufficient data quality, the formation of Fe-O scatterings could not be additionally proven by EXAFS fitting at the Fe K-edge. As the Ni-Ni coordination peak in the FT-EXAFS spectra (Figure S 4) at 2.1 Å increased and the backscattering due to Fe-Fe contributions at 2.1 Å and Fe-Ni at 4.0 Å declined dealloying of the Ni-Fe particles under formation of an Fe/FeO rich surface was found (see next section and paper).

3.2.1 EXAFS fitting details

At the Ni K-edge EXAFS spectra were fitted in the range of R = 1.0-3.2 Å and k = 2.0-11.0 $Å^{-1}$ for the as prepared catalyst and in range of R = 1.0-5.0 Å and k = 2.7-12.5 $Å^{-1}$ for catalyst after TPR . The amplitude reduction factor (S_0^2), as determined from Ni foil, was fixed at 0.84 and one energy shift parameter (E_0) was defined for all scattering paths. Scattering paths Ni-O, and Ni-Ni obtained from reference models were used and parameters N, ΔR and σ^2 were fitted.

At the Fe K-edge EXAFS spectra were fitted in the range of R = 1.0-5.0 Å and k = 2.7-10.5 $Å^{-1}$. The amplitude reduction factor (S_0^2), as determined from Fe foil, was fixed at 0.82 and one energy shift parameter (E_0) was defined for all scattering paths. Scattering paths Fe-Fe (Fe bulk) and Fe-Fe (Ni-Fe alloy) obtained from reference models were used and parameters N, ΔR and σ^2 were fitted.

Simulation of XANES spectra using FEFF9 code

For XANES simulations at Ni K- and Fe K-edges in FEFF9, the ab initio self-consistent real-space Green's function (RSGF) approach was used including inelastic losses, core-hole effects, vibrational amplitudes, etc. The polarization dependence, core-hole effects, and local field corrections were based on self-consistent, spherical muffin-tin scattering potentials. In the present ab-initio calculations, the Hedin-Lundqvist potential was chosen and XANES, Absolute, SCF (self-consistent field), and FMS (full multiple scattering) cards were used. The self-consistent potential (SCF) parameters were as follows: rfms = 5.2, lfms1 = 0, nscmt = 100, ca = 0.2, nmix = 1. The XANES parameters were as follows: xkmax = 4, xkstep = 0.07, vixan = 0. The LDOS card was added for density of states calculation with an energy range of −20 to 30 eV with a Lorentzian broadening with half-width of 0.1 eV.

3.2.1.1 Ni K-edge EXAFS fitting of the Ni-Fe/Al_2O_3 catalyst

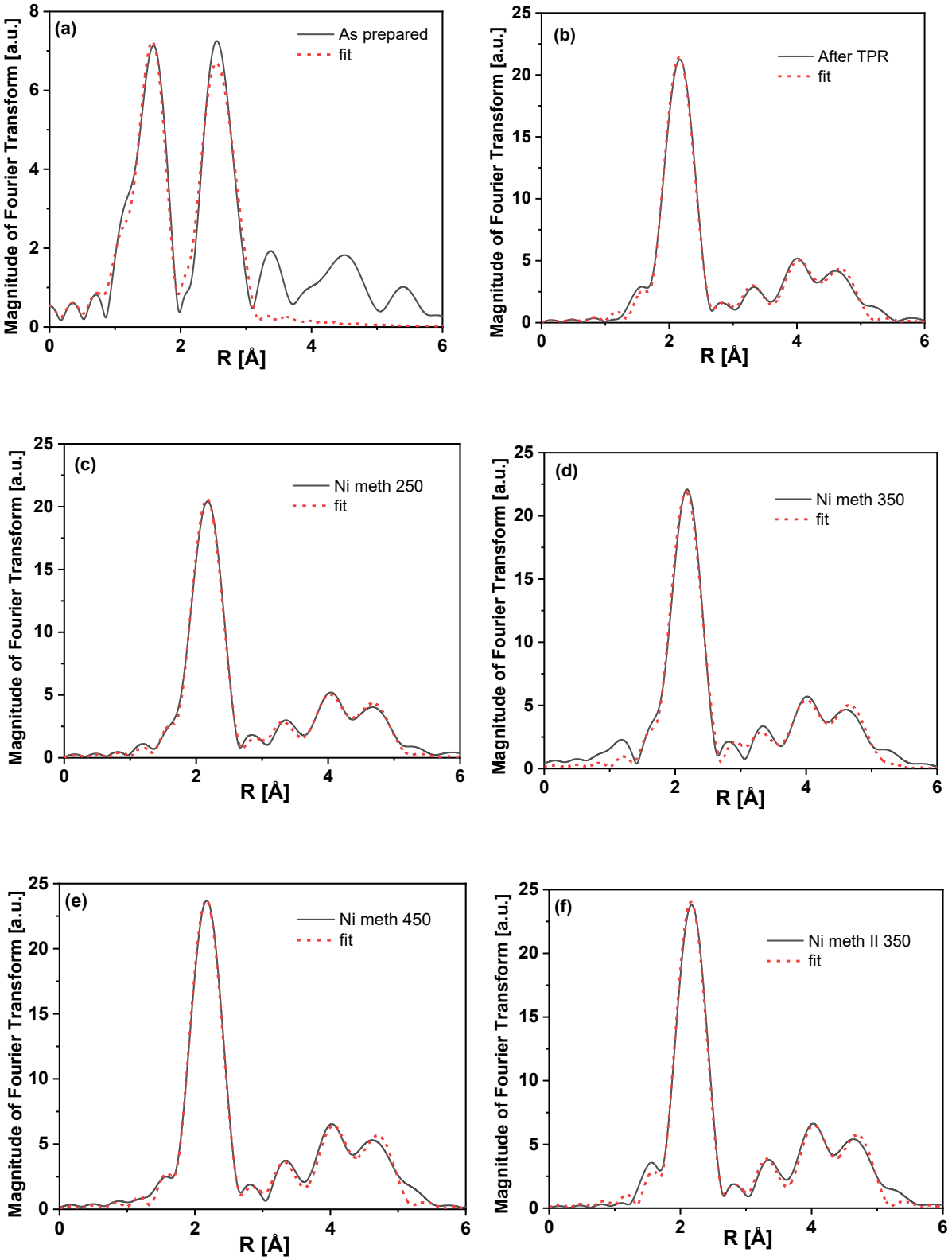

Figure S 5: k^2-weighted Fourier transformed EXAFS (black) and the fit result (red) at the Ni K-edge of the 17 wt.% Ni-Fe/γ-Al_2O_3 catalyst as prepared at 50 °C (a), after H_2-TPR (b), after applying for 1 h methanation conditions of 20 ml/min 50 vol% H_2:CO_2=4:1 in N_2 at atm and 250 °C (c), 350 °C (d), 400 °C (e) and 350 °C II (f). EXAFS fitting results in Table S 1.

3.2.1.8 Fe K-edge EXAFS fitting of the Ni-Fe/Al_2O_3 catalyst after methanation of CO_2 at 250 °C

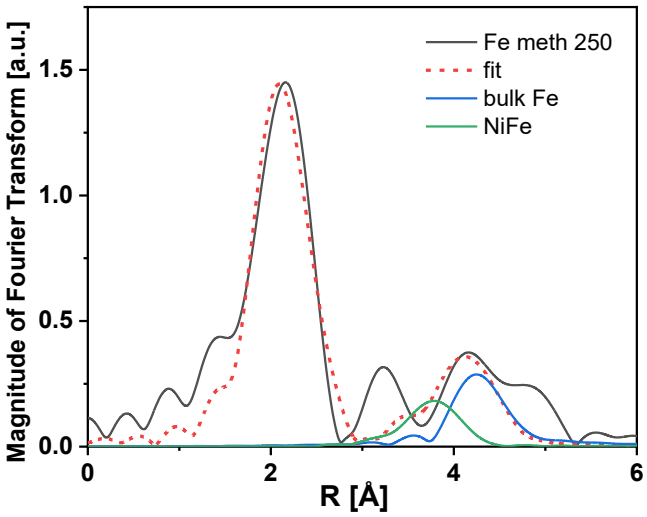

Figure S 6: k^2-weighted Fourier transformed EXAFS (black) and the fitted spectrum (red) at the Fe K-edge of the 17 wt.% Ni-Fe/γ-Al_2O_3 catalyst after CO_2 methanation at 250 °C after applying for 1 h methanation conditions of 20 ml/min 50 vol% H_2:CO_2=4:1 in N_2 at atm and 250 °C (EXAFS fitting results in Table S1).

Table S 1: Structural parameters of the 17 wt.% Ni-Fe/γ-Al_2O_3 catalyst determined of EXAFS spectra at the Ni K-edge , S_0^2 =0.84, data fits are given in Figure S 5.

	Ni-O			Ni-Ni										
	R / Å	CN	DW factor · 10^{-2} / Å^2	R / Å	CN	DW factor · 10^{-2} / Å^2	R / Å	CN	DW factor · 10^{-2} / Å^2	R / Å	CN	DW factor · 10^{-2} / Å^2	χ_v^2 / a.u.	E_0 / eV
As prepared	2.05	5.6 ± 1.2	0.0077 ± 0.0023	2.97	7.6 ± 2.5	0.0117 ± 0.0027							753	-3.7 ± 1.6
	Ni-Ni1			Ni-Ni2			Ni-Ni3			Ni-Ni4				
After TPR	2.50	8.2±1.2	0.0093 ± 0.0017	3.52	6.0 [f]	0.0168 ± 0.0024	4.36	24 [f]	0.0166 ± 0.0010	5.12	12 [f]	0.0088± 0.0013	77	6.9 ± 1.1
Meth 250 °C	2.49	8.0±1.2	0.0090 ± 0.0017	3.52	6.0 f	0.0168 ± 0.0021	4.35	24 [f]	0.0166 ± 0.0011	5.12	12 [f]	0.0096± 0.0014	104	6.6 ± 1.1
Meth 350 °C	2.49	7.2±1.8	0.0062 ± 0.0018	3.51	6.0 f	0.0173 ± 0.0060	4.33	24 [f]	0.0157 ± 0.0026	5.08	12 [f]	0.0102± 0.0027	619	4.8 ± 2.7
Meth 450 °C	2.50	8.4±1.2	0.0086 ± 0.0016	3.53	6.0 f	0.0154 ± 0.0023	4.36	24 [f]	0.0146 ± 0.0008	5.12	12 [f]	0.0069± 0.0011	136	8.4 ± 1.2
Meth II 350 °C	2.50	8.7±1.2	0.0093 ± 0.0016	3.52	6.0 f	0.0147 ± 0.0021	4.36	24 [f]	0.0147 ± 0.0010	5.12	12 [f]	0.0068± 0.0011	137	7.7 ± 1.2

Table S 2: Structural parameters a of the 17 wt.% Ni-Fe/γ-Al_2O_3 catalyst determined of EXAFS spectra t the Fe K-edge spectra, S_0^2 =0.82, data fit is given in Figure 2 and Figure S 6.

	Fe-Fe1			Fe-Fe2			Fe-Fe4			Fe-Fe3 (NiFe)				
	R / Å	CN	DW factor · 10^{-2} / Å^2	R / Å	CN	DW factor · 10^{-2} / Å^2	R / Å	CN	DW factor · 10^{-2} / Å^2	R / Å	CN	DW factor · 10^{-2} / Å^2	χ_v^2 / a.u.	E_0 / eV
After TPR	2.50	6.1±1.2	0.0075 ± 0.0017	2.89	2.0 [f]	0.0075 ± 0.0017	4.79	4 [f]	0.0031 ± 0.0003	4.36	4 [f]	0.0128 ± 0.0124	237	4.4 ± 2.6
Meth 250 °C	2.48	4.4±1.1	0.0080 ± 0.0020	2.85	2.0 [f]	0.0080 ± 0.0020	4.72	3 [f]	0.0043 ± 0.0027	4.29	4 [f]	0.0122 ± 0.0093	95	-2.9 ± 3.7

f – fixed during fitting

3.2.2 Rietveld refinement of synchrotron-based powder XRD

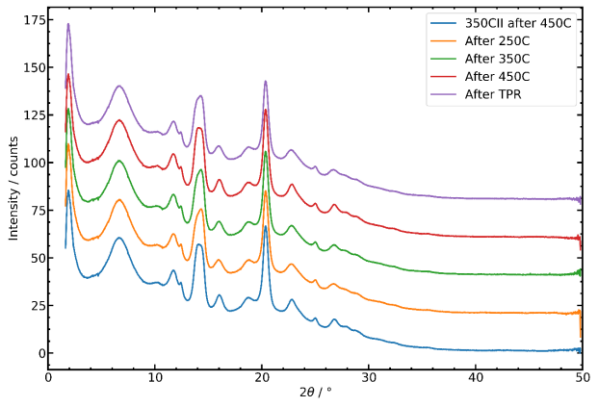

Figure S 7: Stacked diffraction patterns (λ = 0.4943 Å) for different stages of the catalysts used for Rietveld refinement over the whole measured angular scale. A 2θ range from 10 to 30 ° was used for Rietveld refinements. Broad reflections at 7 ° are caused by the quartz capillary. After H_2-TPR (purple); after 1 h methanation of CO_2 at 250 °C (orange), 350 °C (green), 450 °C (red) and a subsequent second step at 350 °C (blue).

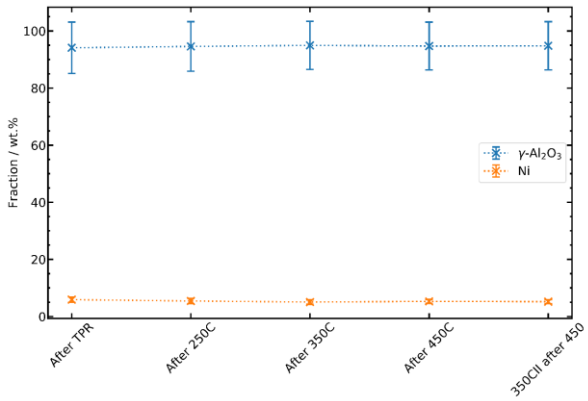

Figure S 8: Fractions obtained from Rietveld refinement for γ-Al_2O_3 and Ni phases for different stages of the catalysts. Values should be only interpreted qualitatively, standard deviations for γ-Al_2O_3 phase are quite large.

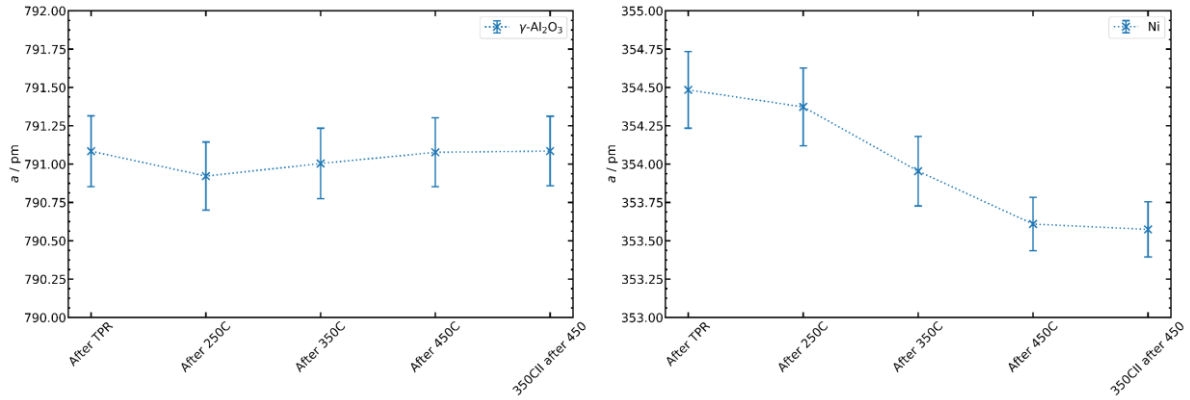

Figure S 9: Lattice parameter *a* with standard deviation of γ-Al_2O_3 phase (left) and Ni phase (right) as obtained by Rietveld refinement for different stages of the catalysts.

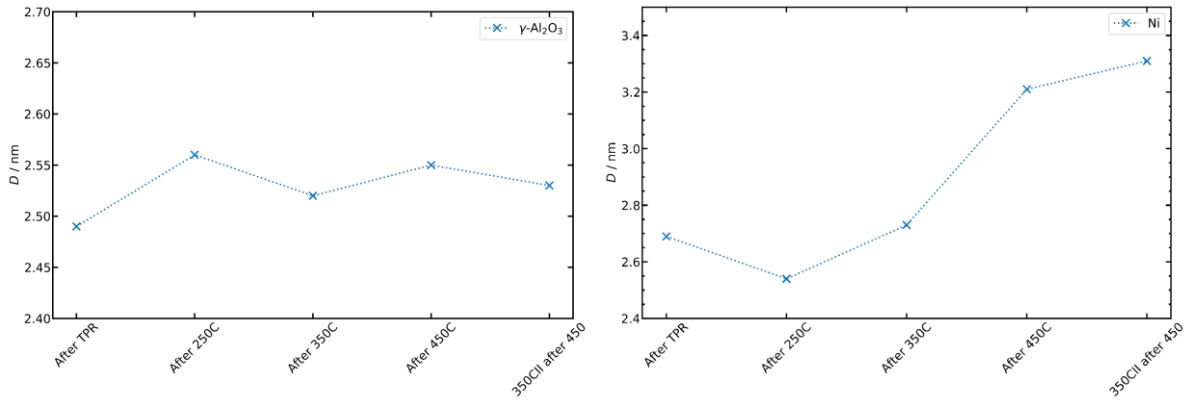

Figure S 10: Crystallite sizes *D* of γ-Al_2O_3 (left) and Ni phase (right) as obtained by Rietveld refinement for different stages of the catalysts.

3.2.2.1 Rietveld refinement of the XRD data obtained from the Ni-Fe catalyst after H_2-TPR

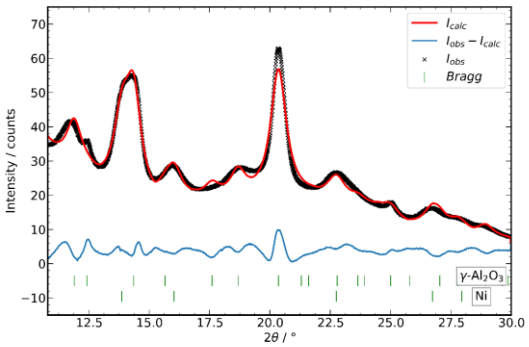

Figure S 11: Rietveld refinement after TPR; black crosses measured intensity, red calculated intensity and blue difference between measured and calculated intensity, green lines are Bragg marker. Bragg marker top: γ-Al_2O_3; Bragg marker bottom: Ni; R_{wp}: 4.61; R_p: 3.72; S: 0.23.

Table S 3: Structural data obtained from Rietveld refinement after TPR.

Phase	Ni	γ-Al_2O_3
Space group	*Fm*-3*m* (No. 225)	*Fd*-3*m* (No. 227)
a in pm	354.4(3)	791.1(2)
D in nm	2.69	2.49
ε in %	5.76	0.31
Fraction in wt.%	5.9(9)	94(9)

Phase		Ni			
atom	*x*	*y*	*z*	B_{iso}	*occ*
Ni	0	0	0	0.300	0.021

Phase		γ-Al_2O_3			
atom	*x*	*y*	*z*	Bi_{so}	*occ*
O1	0.2583(18)	0.2583(18)	0.2583(18)	1.000	0.167
Al1	½	½	½	0.500	0.048
Al2	⅛	⅛	⅛	0.500	0.035
Al3	0.014(6)	0.014(6)	0.014(6)	0.500	0.028

3.2.2.2 Rietveld refinement of the XRD data obtained from the Ni-Fe catalyst after methanation at 250 °C

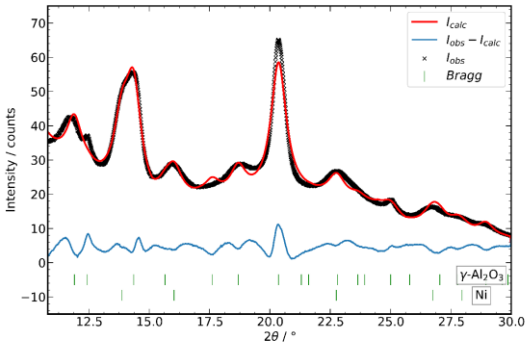

Figure S 12: Rietveld refinement after the methanation step at 250 °C; black crosses measured intensity, red calculated intensity and blue difference between measured and calculated intensity, green lines are Bragg marker. Bragg marker top: γ-Al_2O_3; Bragg marker bottom: Ni; R_{wp}: 4.80; R_p: 3.88; S: 0.25.

Table S 4: Structural data obtained from Rietveld refinement after the methanation step at 250 °C.

Phase	Ni	γ-Al_2O_3
Space group	*Fm*-3*m* (No. 225)	*Fd*-3*m* (No. 227)
a in pm	354.3(3)	790.9(2)
D in nm	2.54	2.56
ε in %	3.06	0.30
Fraction in wt.%	5.4(9)	95(9)

Phase		Ni			
atom	*x*	*y*	*z*	B_{iso}	*occ*
Ni	0	0	0	0.300	0.021

Phase		γ-Al_2O_3			
atom	*x*	*y*	*z*	B_{iso}	*occ*
O1	0.2586(17)	0.2586(17)	0.2586(17)	1.000	0.167
Al1	½	½	½	0.500	0.048
Al2	⅛	⅛	⅛	0.500	0.035
Al3	0.012(6)	0.012(6)	0.012(6)	0.500	0.028

3.2.2.3 Rietveld refinement of the XRD data obtained from the Ni-Fe catalyst after methanation at 350 °C

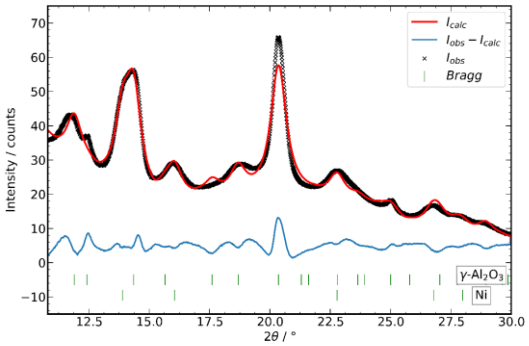

Figure S 13: Rietveld refinement after the methanation step 350 °C; black crosses measured intensity, red calculated intensity and blue difference between measured and calculated intensity, green lines are Bragg marker. Bragg marker top: γ-Al_2O_3; Bragg marker bottom: Ni; R_{wp}: 5.02; R_p: 3.96; S: 0.26.

Table S 5: Structural data obtained from Rietveld refinement after the methanation step at 350 °C.

Phase	Ni	γ-Al_2O_3
Space group	*Fm*-3*m* (No. 225)	*Fd*-3*m* (No. 227)
a in pm	353.9(2)	791.0(2)
D in nm	2.73	2.52
ε in %	1.80	0.30
Fraction in wt.%	5.1(8)	95(8)

Phase		Ni			
atom	*x*	*y*	*z*	B_{iso}	*occ*
Ni	0	0	0	0.300	0.021

Phase		γ-Al_2O_3			
atom	*x*	*y*	*z*	B_{iso}	*occ*
O1	0.2587(17)	0.2587(17)	0.2587(17)	1.000	0.167
Al1	½	½	½	0.500	0.048
Al2	⅛	⅛	⅛	0.500	0.035
Al3	0.013(5)	0.013(5)	0.013(5)	0.500	0.028

3.2.2.4 Rietveld refinement of the XRD data obtained from the Ni-Fe catalyst after methanation at 450 °C

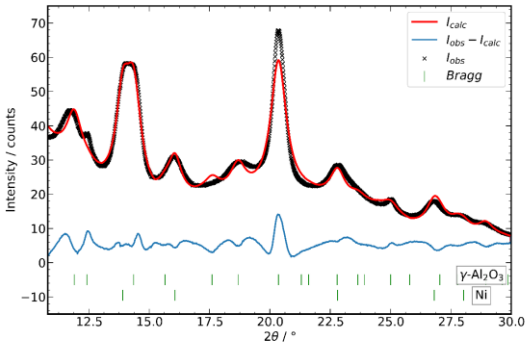

Figure S 14: Rietveld refinement after the methanation step at 450 °C; black crosses measured intensity, red calculated intensity and blue difference between measured and calculated intensity, green lines are Bragg marker. Bragg marker top: γ-Al_2O_3; Bragg marker bottom: Ni; R_{wp}: 5.14; R_p: 4.03; S: 0.27.

Table S 6: Structural data obtained from Rietveld refinement after the methanation step at 450°C.

Phase	Ni	γ-Al_2O_3
Space group	*Fm*-3*m* (No. 225)	*Fd*-3*m* (No. 227)
a in pm	353.61(17)	791.1(2)
D in nm	3.21	2.55
ε in %	2.17	0.30
Fraction in wt.%	5.3(7)	95(8)

Phase		Ni			
atom	*x*	*y*	*z*	B_{iso}	*occ*
Ni	0	0	0	0.300	0.021

Phase		γ-Al_2O_3			
atom	*x*	*y*	*z*	B_{iso}	*occ*
O1	0.2585(17)	0.2585(17)	0.2585(17)	1.000	0.167
Al1	½	½	½	0.500	0.048
Al2	⅛	⅛	⅛	0.500	0.035
Al3	0.015(5)	0.015(5)	0.015(5)	0.500	0.028

3.2.2.5 Rietveld refinement of the XRD data obtained from Ni-Fe catalyst after methanation at 350 °C II

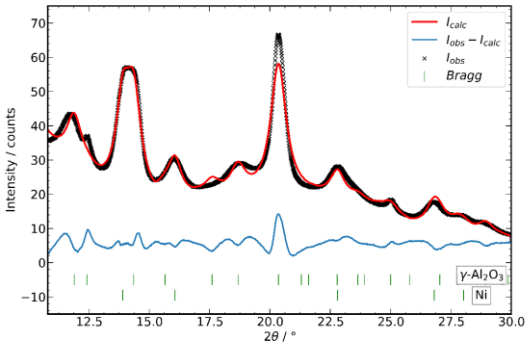

Figure S 15: Rietveld refinement after the methanation step at 350 °C subsequent to 450 °C; black crosses measured intensity, red calculated intensity and blue difference between measured and calculated intensity, green lines are Bragg marker. Bragg marker top: γ-Al_2O_3; Bragg marker bottom: Ni; R_{wp}: 5.13 %; R_p: 4.00 %; S: 0.26.

Table S 7: Structural data obtained from Rietveld refinement of after the methanation step at 350 °C subsequent to 450 °C.

Phase	Ni	γ-Al_2O_3
Space group	*Fm*-3*m* (No. 225)	*Fd*-3*m* (No. 227)
a in pm	353.57(18)	791.1(2)
D in nm	3.31	2.53
ε in %	2.97	3.02
Fraction in wt.%	5.2(7)	95(8)

Phase		Ni			
atom	*x*	*y*	*z*	B_{iso}	*occ*
Ni	0	0	0	0.300	0.021

Phase		γ-Al_2O_3			
atom	*x*	*y*	*z*	B_{iso}	*occ*
O1	0.258(17)	0.258(17)	0.258(17)	1.000	0.167
Al1	½	½	½	0.500	0.048
Al2	⅛	⅛	⅛	0.500	0.035
Al3	0.015(5)	0.015(5)	0.015(5)	0.500	0.028

3.3 Development of a structural model

To develop the structural model, it is important to understand how the surface composition changes. The number and composition of nickel and iron atoms in the particle and on the surface was estimated (Table S 8).

Table S 8: Calculation of atoms and surface atoms of the Ni-Fe catalyst after TPR and at various temperatures during CO_2 methanation.

Number Atoms	**ATPR**	**250 °C**	**350 °C**	**450 °C**	**350 °C II**
Total Ni+Fe	1660 ± 1000	1400 ± 850	1730 ± 1050	2800 ± 1660	3060 ± 1810
Total Ni	1380 ± 860	1180 ± 740	1500 ± 920	2480 ± 1490	2710 ± 1620
Total Fe	320 ± 210	270 ± 180	270 ± 180	350 ± 230	390 ± 250
Surface	390 ± 170	350 ± 150	400 ± 170	550 ± 230	590 ± 250
Surface Ni	320 ± 150	280 ± 120	290 ± 130	350 ± 150	370 ± 160
Surface Fe	70 ± 40	70 ± 30	130 ± 80	220 ± 130	240 ± 150
Oxidized Fe	-	50 ± 40	120 ± 80	180 ± 120	190 ± 120

The error margin in the obtained numbers of atoms is quite high due to the error of ± 0.9 in the particle size of 3.9. However, the numbers give a good trend how surface and particle composition change. Based on the estimation, the amount of iron at the surface strongly increases with temperature. The iron on the surface is nearly fully oxidized as soon as CO_2 methanation conditions were applied.

3.4 Catalyst response to periodic CO_2 feed modulations (MES)

3.4.1 Steady state of Ni/Al_2O_3 and $Ni-Fe/Al_2O_3$ before and after the MES experiment

The overall catalyst performance (Table S 9) reflected the trends observed in previous studies with comparison between Ni and Ni-Fe catalysts.[11-13]

Table S 9: Conversion and yields of the Ni/Al_2O_3 and the $Ni-Fe/Al_2O_3$ catalyst at 250 °C and 450 °C before and after the MES experiments. The conversions were normalized to the average catalyst mass of 4.4 mg obtained from our capillary reactor with a catalyst bed of 1 cm length and 1.5 mm diameter.

Ni	250 °C		350 °C		450 °C	
	Before MES	After MES	Before MES	After MES	Before MES	After MES
$X(CO_2)$	2 %	2 %	33 %	33 %	49 %	49 %
$S(CH_4)$	69 %	69 %	54 %	53 %	78 %	76 %

Ni-Fe	250 °C		350 °C		450 °C	
	Before MES	After MES	Before MES	After MES	Before MES	After MES
$X(CO_2)$	3 %	3 %	37 %	38 %	49 %	48 %
$S(CH_4)$	53 %	50 %	78 %	81 %	79 %	79 %

At 250 °C, a slightly higher CO_2 conversion of 3 % was observed for the Ni-Fe catalyst compared to 2 % of the unpromoted Ni catalyst. However, the selectivity was better for the unpromoted sample reaching 69 % compared to 53 % of the Ni-Fe catalyst. When the temperature was increased to 450 °C, both catalysts provided a CO_2 conversion of 49 % and a selectivity to CH_4 of ~ 78 %. Note, that the CO formation was much more pronounced in this experiment compared to the literature and our previous studies under stationary conditions, as we applied in this case a $WHSV_{total}$ = 684000 ml/(g_{cat}*h) to ensure fast changes of the reactant gases in the catalyst bed during the MES experiments. The conversion profiles provided evidence that there was no major catalyst deactivation after the MES experiments suggesting that possible changes during the modulations were reversible.

3.4.2 Ni K-edge XANES spectra of Ni/Al_2O_3 and $Ni-Fe/Al_2O_3$ before the MES experiment

The normalized XANES spectra at the Ni K-edge after reaching the steady state of the catalyst during methanation of CO_2 at various temperatures are shown in Figure S 16 for Ni and Ni-Fe, respectively.

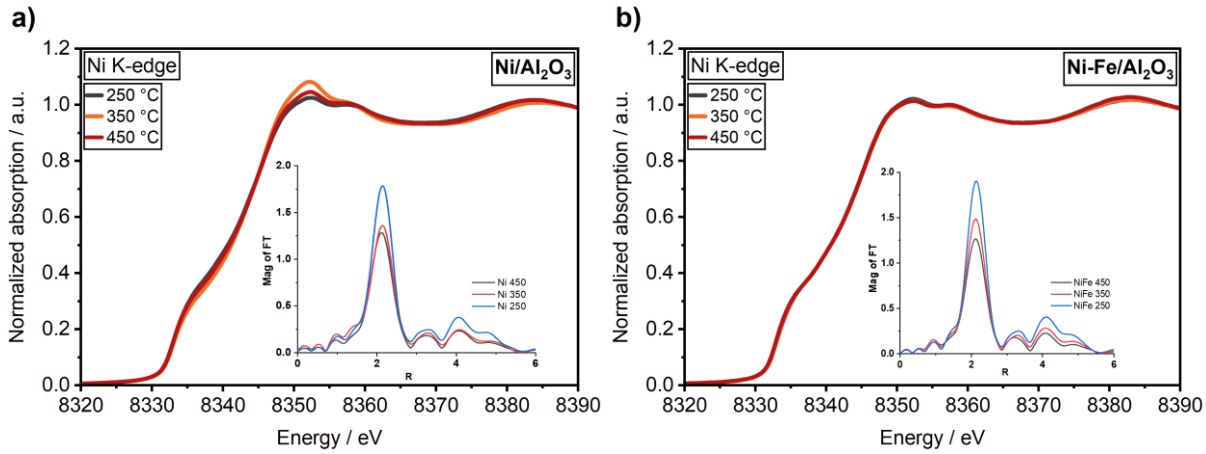

Figure S 16: XANES spectra recorded in transmission mode and k^2-weighted Fourier transformed EXAFS (inset) at the Ni K-edge of the (a) 17 wt.% $Ni/\gamma\text{-}Al_2O_3$ and (b) 17 wt.% $Ni_3Fe/\gamma\text{-}Al_2O_3$ catalyst at 250 °C (black), 350 °C (orange) and 450 °C (red) during methanation of CO_2 in 50 ml/min 25 vol% H_2:CO_2=4:1 in N_2 at atm prior to the MES experiment.

For the unpromoted Ni catalyst, at 250 °C (Figure S 16a, grey), Ni was mostly in reduced metal phase with some partial oxidation during the methanation of CO_2. The corresponding FT EXAFS spectra shown in the inset further substantiated that Ni remained in its reduced sate. A coordination number (CN) of 7.6 ± 1.0 for Ni-Ni scattering was estimated and no Ni-O contribution was observed.

At 350 °C, an increase in the intensity of white line and a slight shift of the edge towards higher energy were found indicating a higher amount of oxidized Ni species (Figure S 16a, orange). Note, that this might partially be due to an experimental error during the reduction procedure (different H_2:N_2 ratio). A contribution from Ni-O was found in the FT EXAFS spectra (Figure S 16a, inset). The CN of Ni-Ni remained unchanged at 7.6 ± 1.2 compared to the steady state at 250 °C.

In the steady state at 450 °C, the intensity of the white line was also slightly increased, and the edge shifted to higher energy compared to the state at 250 °C. The EXFAS fitting results at 450 °C, with a CN of 8.8 ± 1.3 for Ni-Ni scattering at 2.45 Å and weak contribution from Ni-O at 2.02 Å (fixed CN =1) points towards contribution from Ni-O species which may be due to some Ni species in oxidized phase.

The steady state of the Ni-Fe catalyst (Figure S 16b) was already discussed in the main article. The states before MES are displayed here to confirm the previous results. It should be mentioned, that in contrast to the unpromoted sample, Ni remained in its reduced state during all temperature steps. The EXAFS analysis demonstrated that the CN of Ni-Ni scattering at 2.45 Å in the bimetallic Ni-Fe catalyst were 8.8 ± 1.4, 8.8 ± 1.2 and 8.5 ± 0.8 at 450 °C, 350 °C and 250 °C, respectively. This was in a good

agreement with the results provided in the main article. In comparison to the unpromoted Ni catalyst, the addition of Fe resulted in a weaker contribution from Ni-O at 350 °C and 450 °C. Hence, Ni was comparatively more reduced in presence of Fe and more stable during the methanation of CO_2 at different temperatures.

3.4.3 Fe K-edge XANES spectra of Ni/Al_2O_3 and $Ni-Fe/Al_2O_3$ before the MES experiment

The changes occurring during MES can depend on the steady state of the catalyst before MES. Figure S 17a shows the normalized XANES spectra at Fe K-edge for the steady state of the catalyst before MES experiment at different temperatures.

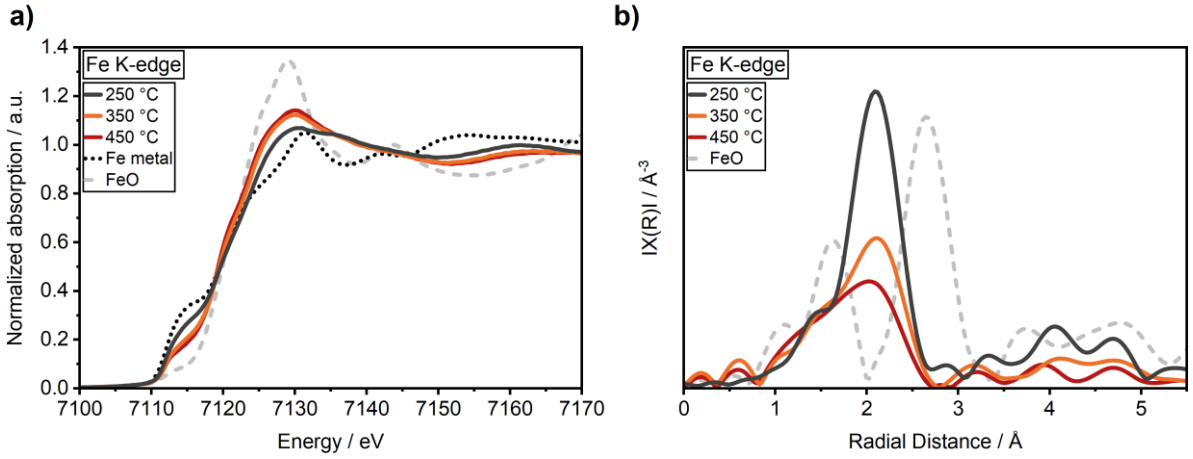

Figure S 17: XANES spectra recorded in transmission mode (a) and k^2-weighted Fourier transformed EXAFS (b) at the Fe K-edge of the 17 wt.% Ni_3Fe/γ-Al_2O_3 catalyst at 250 °C (black), 350 °C (orange) and 450 °C (red) during methanation of CO_2 in 50 ml/min 25 vol% H_2:CO_2=4:1 in N_2 at atm prior to the MES experiment.

At 250 °C, Fe was mostly in reduced metal phase with some partial oxidation, however at 350 °C the increase in the intensity of white line and shift of the edge towards higher energy indicate that more Fe species are present in oxidized phase, i.e., FeO. The degree of oxidation increases further at 450 °C showing effect of temperature on oxidation state of Fe. The changes in the XANES spectra can be further confirmed in the corresponding FT EXAFS spectra shown in Figure S 17b where contribution from of Fe-O scattering at ~ 1.6 Å observed as shoulder to the first scattering peak Fe-Fe grows with increasing temperature indicating high oxidation of Fe species. From EXAFS fitting, the CN of Fe-O scattering at 1.96 Å were found to be 1.2 ± 0.3, 1.7 ± 0.6 and 3.5 ± 1.2 at 250 °C, 350 °C and 450 °C, respectively. Hence, at higher temperatures Fe is more oxidized in its steady state before MES.

3.4.5 Time-resolved XANES spectra of the monometallic Ni/Al₂O₃ catalyst

Time-resolved XANES spectra obtained from 30 periods averaged into one period (a total of 24 spectra) and the corresponding phase-resolved spectra obtained during the experiment performed at 450 °C are given in Figure S 18.

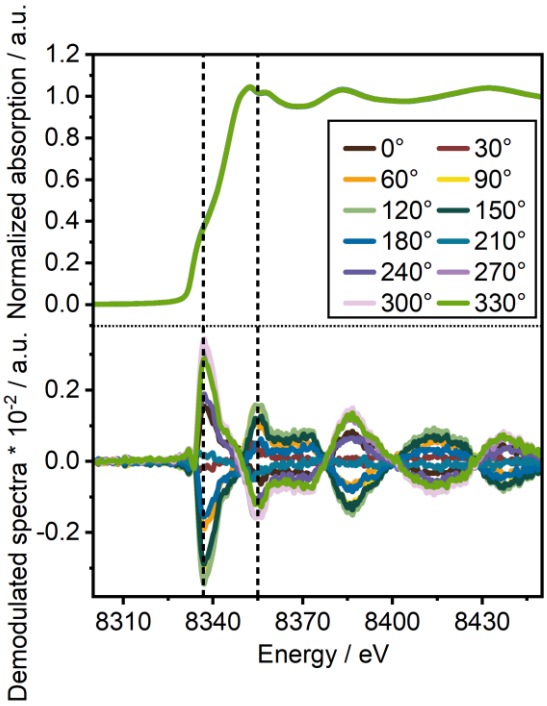

Figure S 18: Normalized time-resolved Ni K-edge XANES (top) and corresponding demodulated spectra (bottom), at selected values of phase angle ($\Delta\phi$) consisting of a total of 24 spectra covering 5 seconds each for the 17 wt.% Ni/γ-Al_2O_3 catalyst during $CO_2/H_2/N_2$ (0-60 s) vs. H_2/N_2 (60-120 s) cycling and 30 periods average (bottom).

3.4.6 Time-resolved XANES spectra of the bimetallic Ni-Fe/Al_2O_3 catalyst

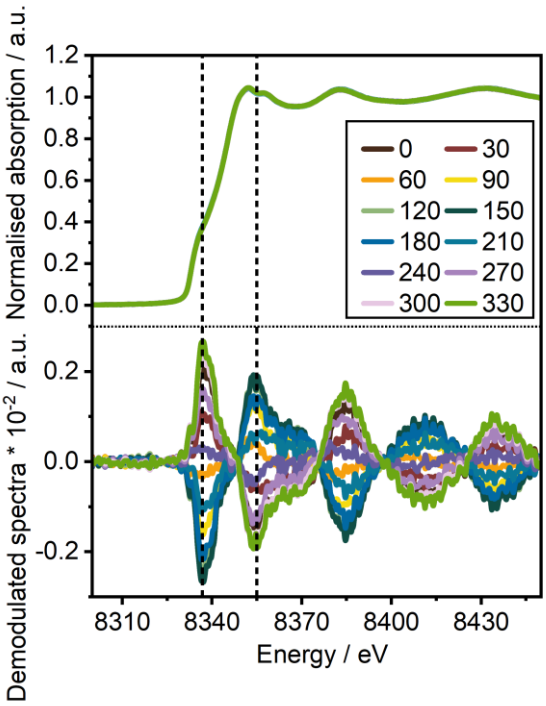

Figure S 19: Normalized time-resolved Ni K-edge XANES (top) and corresponding demodulated spectra (bottom) at selected values of phase angle ($\Delta\phi$) consisting of a total of 24 spectra covering 5 seconds each for the 17 wt.% Ni-Fe/γ-Al_2O_3 catalyst during $CO_2/H_2/N_2$ (0-60 s) vs. H_2/N_2 (60-120 s) cycling and 30 periods average (bottom).

3.4.7 Phase-resolved Ni K-edge MES spectra of Ni/Al_2O_3 and $Ni-Fe/Al_2O_3$ catalyst

First, the monometallic Ni/Al_2O_3 catalyst was investigated. No distinct changes were visible in the characteristic features of the conventional time-resolved Ni K-edge XANES spectra (Figure S 18b).

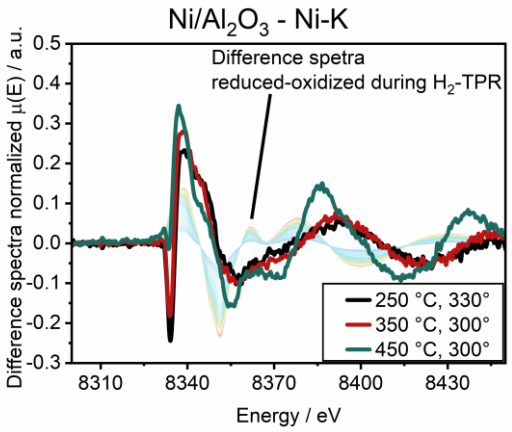

Figure S 20: Comparison of the difference spectrum obtained at the Ni K-edge during H_2-TPR with the demodulated spectra of maximum amplitude at 250 °C, 350 °C and 450 °C.

The demodulated spectra obtained at 250 °C, 350 °C and 450 °C in comparison to the difference spectra collected during H_2-TPR (Ni-NiO) are displayed in Figure S 20. The comparison did not result in a good match. This demonstrates that complex structural changes are occurring at the Ni K-edge of the monometallic Ni catalyst.

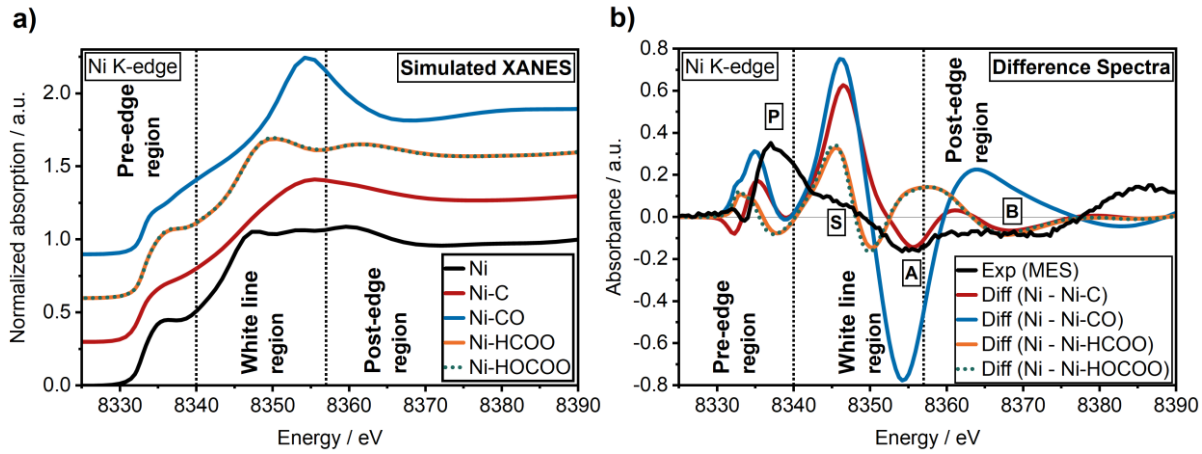

Figure S 21: (a) Simulated Ni K-edge XANES spectra for the DFT simulated structure for C (red), CO (blue), HCOO (orange) and HOCOO (green, dotted) substitution on the reduced Ni structure. (b) Comparison of the obtained difference spectrum from these theoretical XANES spectra with simulated pure Ni metal spectrum to the experimentally obtained demodulated spectrum at 450 °C, 300°.

One representative curve of the changes after the demodulation of the Ni/Al_2O_3 catalyst at 450 °C and a phase angle of 300° recorded at the Ni K-edge is displayed in Figure S 21.

In order to interpret the features of the demodulated spectrum, XANES spectra for DFT calculated structures of Ni surface with different species, *i.e.*, Ni-C, Ni-CO, Ni-HCOO and Ni-HOCOO have been simulated using FEFF9 as shown in Figure S 21a along with simulated Ni metal spectrum. Their corresponding difference spectra with the simulated Ni metal spectrum were calculated and compared to our experimental demodulated spectrum (Figure S 18b, black curve). Four features were observed in the experimental spectrum, and denoted as ***P***, ***S***, ***A*** and ***B***, respectively. Feature ***P*** at ~ 8334 eV (pre-edge region) correlated well to the difference spectra of Ni-NiC and Ni-NiCO, although shifted to slightly higher energy. The shoulder ***S*** at around 8345 eV was found in all references. However, the shoulder feature was not intense in the experimental data indicating the contribution of Ni-HCOO/Ni-HOCOO species, as the shoulder was less intense for these species compared to Ni-C / Ni-CO. The formation of Ni-HCOO/Ni-HOCOO species would be in a good agreement to DRIFTS studies[14-16] on Ni based catalysts. After the white line region, feature ***A*** at 8355 eV in the post edge region further substantiated the formation of Ni-C / Ni-CO species, as already suggested by feature ***P***. However, feature ***B*** at 8368 eV correlated rather more to Ni-C than Ni-CO. Hence, the dissociative pathway of CO_2 activation seems to be preferred on the monometallic Ni/γ-Al_2O_3 catalyst at 450 °C.

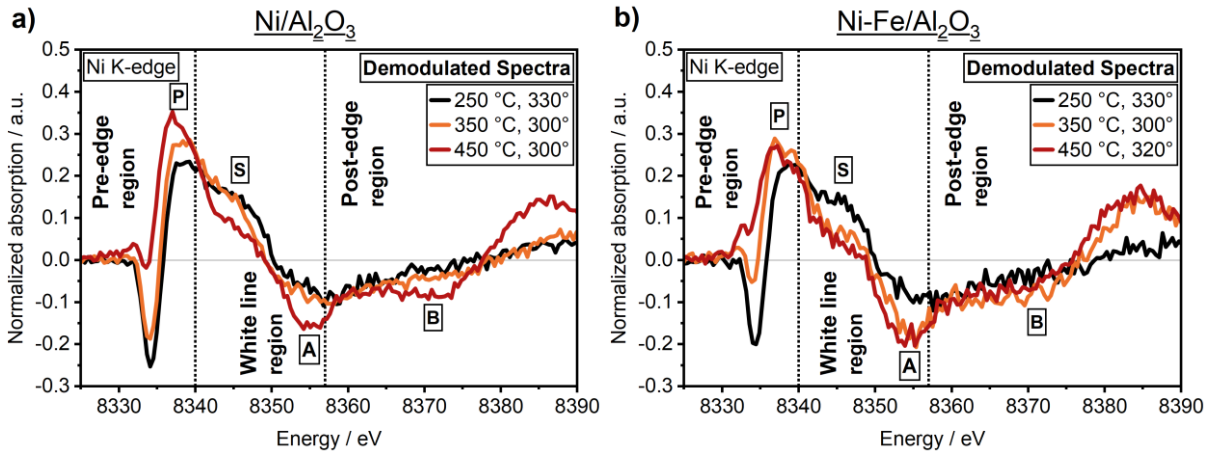

Figure S 22: Demodulated Ni K-edge spectra of the 17 wt.% Ni/γ-Al_2O_3 (a) and the 17 wt.% Ni-Fe/γ-Al_2O_3 (b) catalyst at 250 °C (black), 350 °C (orange) and 450 °C (red) during $CO_2/H_2/N_2$ (0-60 s) vs. H_2/N_2 (60-120 s) cycling with 30 periods average.

The demodulated spectra of both catalysts with the highest amplitude at the Ni K-edge at 250 °C, 350 °C and 450 °C have been plotted in Figure S 22. On the monometallic Ni catalyst in Figure S 22a an increase in temperature resulted in a sharpening of the pre-edge feature ***P***. This indicated a preferred formation of Ni-C or Ni-CO species during CO_2 modulations at higher temperatures. However, feature ***B*** only is formed, when the amount of Ni-CO species is decreased (see Figure S 21b) due to a higher fraction of Ni-C or Ni-HCOO / Ni-HOCOO species. Hence, the formation of feature ***B*** in addition to the increasing feature ***P*** demonstrated that the intermediates shifted from Ni-CO to Ni-C at elevated reaction temperatures on the monometallic Ni/γ-Al_2O_3 catalyst. The fact that feature ***A*** did not flatten with the formation of feature ***B*** further substantiated the formation of Ni-C, especially at 450 °C (Figure S 22a).

As feature ***S*** did decrease, although more Ni-C species were formed at higher temperatures, Ni-HCOO / Ni-HOCOO species must be present and formed with an increasing ratio. Hence, we can conclude that in the investigated temperature regime all mentioned species were present during the methanation of CO_2 on the monometallic Ni catalyst. The following relative trends were observed: At 250 °C, preferably Ni-CO was formed. At 350 °C, the amount of Ni-CO was decreased accompanied by an increase in the amount of Ni-HCOO / Ni-HOCOO and Ni-C. By further increasing the temperature to 450 °C the amount of Ni-CO further decreased and a distinct formation of Ni-HCOO / Ni-HOCOO and Ni-C was observed.

The same experiment was performed on the bimetallic Ni-Fe sample (Figure S 19). The demodulated spectra of the Ni K-edge with the highest amplitude at 250 °C, 350 °C and 450 °C are displayed in Figure S 22b (overview on all phase angles is given in Figure S 23).

At 250 °C, the shape of the demodulated spectrum was similar to the unpromoted sample. This demonstrates that the origin in the difference in catalytic activity at 250 °C can be traced back to reactions on iron sites. With increasing reaction temperature, the feature intensity of ***P*** and ***A*** increased while shoulder ***S*** was declined (Figure S 22b). As discussed for the monometallic Ni sample, a higher intensity of feature ***P*** and ***B*** correlates to the formation of Ni-CO and/or Ni-C. In the demodulated spectra of the Ni-Fe catalyst at 350 °C and 450 °C feature ***A*** was more pronounced compared to the Ni catalyst without pronounced changes in feature ***B***. This suggests a higher ratio of Ni-CO species on the bimetallic Ni-Fe catalyst. Feature ***S*** was distinctly hampered already at 350 °C suggesting the formation of Ni-HCOO / Ni-HOCOO. As this was not observed at 350 °C on the monometallic Ni catalyst (Figure S 22a), where we determined a lower catalytic activity (see Table S 9), these might be crucial intermediates in the methanation of CO_2.

However, none of the simulated references fitted precisely to experimentally obtained data. Although we can get clues on the intermediate species forming on the active sites during CO_2 methanation, the interpretation of the MES signals is still fragile to draw conclusive statements. Nevertheless, we can conclude with certainty that we have no indication of Ni-O species formed and the complex MES analysis demonstrate that processes on Ni are complex with response signal consisting of several C-containing intermediates/structures that give hints on the reaction mechanism.

3.5 Calculations on the stability of the Ni-Fe alloy and formation of FeO_x clusters

3.5.1 Defining U value for GGA+U method

We applied the GGA+U method in order to better describe delocalized iron d orbitals and obtain more accurate energies. Based on the value of the FeO heat of formation compared to metallic Fe[17], we have applied different U values to find the best fit for the experimental data and found a U of 2.7 eV to be optimal.

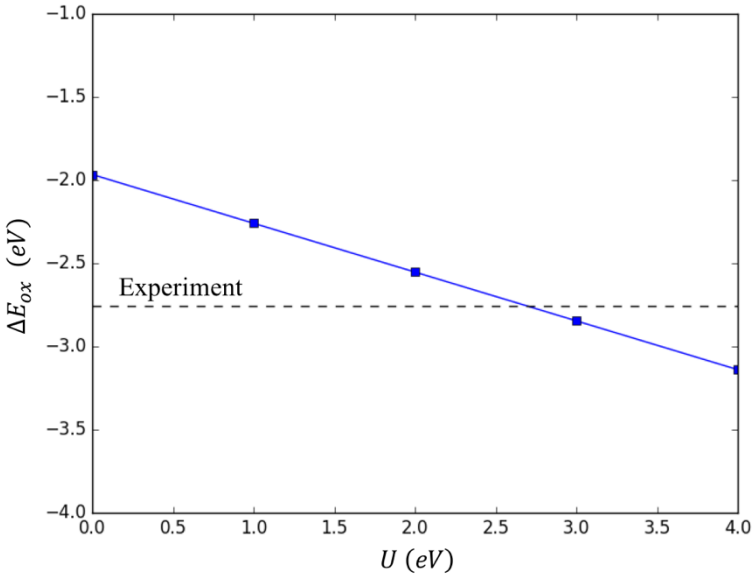

Figure S 23: Calculated heat of FeO formation as a function of U value

3.5.2 Oxygen adsorption on $Ni_4Fe(111)$ alloy

To address the segregation of Fe in the Ni_3Fe alloy during the CO_2 hydrogenation process we constructed a $Ni_4Fe(111)$ slab with the dimension 5x2 in x and y direction. We also take this slab to study FeO ontop of the Ni-Fe alloy. The orthogonal orientation of this unit cell provides close to perfect lattice match in the y direction (4.366 Å) with the FeO lattice parameter (4.363 Å).

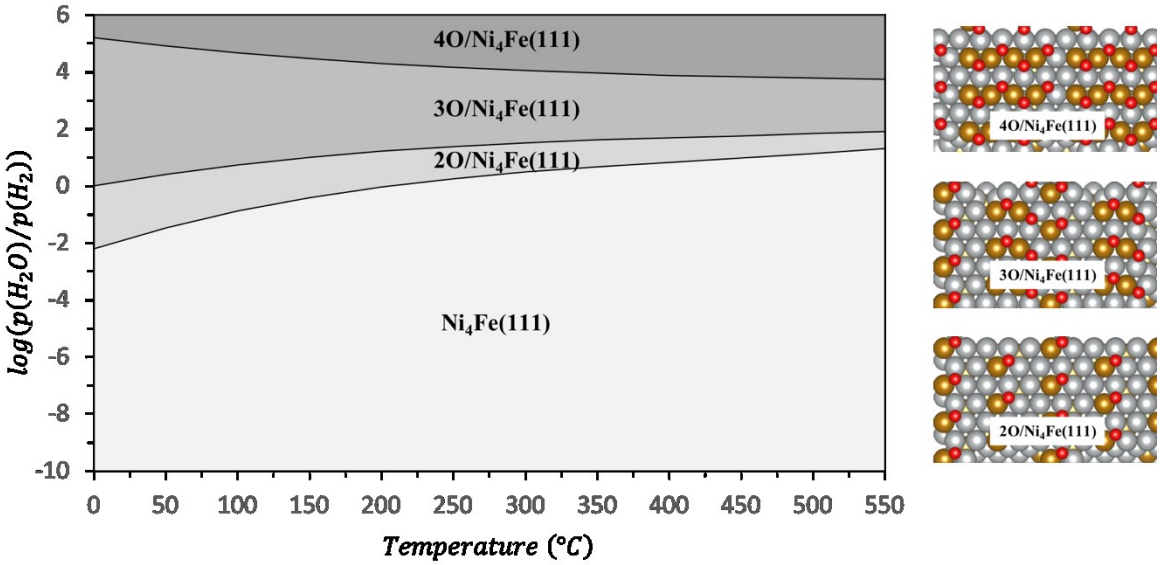

Figure S 24: Phase diagram of xO/$Ni_4Fe(111)$ system as a function of the pH_2O / pH_2 ratio and for temperature range between 0 and 550 °C.

Figure S 24 shows the phase diagram of the Ni-Fe alloy as a function of the oxygen chemical potential expressed as through the H_2O/H_2 ratio. As can be seen in Figure S 24 oxygen adsorption is favorable at higher H_2O/H_2 ratios and leads to the segregation of Fe to the surface of the NiFe alloy.

3.5.3 Carbon monoxide adsorption on $Ni_3Fe(111)$ alloy and $Ni^{top\ layer}/Ni_3Fe(111)$

We tested the effect of Fe on the CO adsorption energy using a stoichiometric Ni-Fe alloy ($Ni_3Fe(111)$) as well as Fe in the sublayers ($Ni^{top\ layer}/Ni_3Fe(111)$). Our calculations indicate that this does not affect the CO or H binding strength (see Table A). However, the presence of oxygen at the surface will reduce the CO binding energy through repulsive adsorbate-adsorbate interactions (see Table A).”

Table S 10: Zero point energy corrected binding energy at (2x2) large unit cells of Ni(111), Ni(111) surface layer over $Ni_3Fe(111)$ three sublayers and $Ni_3Fe(111)$, of: 0.25 ML atomic hydrogen, 0.25 ML CO, CO differential binding energy at 0.50 ML CO, CO referenced to CO+O.

eV	H	CO	2CO-differential	CO $(CO+O)^{ref}$
Ni(111)	-0.31	-1.54	-1.33	-1.03
$Ni^{top\ layer}/Ni_3Fe(111)$	-0.30	-1.52	-1.42	-1.13
$Ni_3Fe(111)$	-0.37	-1.59	-1.41	-0.94

3.5.4 (FeO)x/Ni$_4$Fe(111) surface model*

We further investigated oxidation of metallic Fe to FeO that segregates to the surface of the Ni$_4$Fe(111) alloy. Such particles are modeled as nanowires with different numbers of FeO units in x direction, infinitely repeated in y direction (see also above).

In this model, the oxidation is modeled through segregation of Fe from the alloy to the surface where the alloy is correspondingly depleted of Fe, this is referred to as Ni$_4$Fe(111)*. We choose such a model because it is assumed that the bulk of the alloy will mostly remain the same and that near surface Fe will segregate to the surface and form FeO nanoparticles. Due to the stronger Fe interaction with oxygen compared to Ni, surface Fe atoms are placed underneath the (FeO)x nanowire.

(FeO)$_2$/Ni$_4$Fe(111)* is the smallest studied nanowire. Such a nanowire is less stable than 0.2 and 0.3 ML O/Ni$_4$Fe(111). Slightly larger (FeO)$_3$/Ni$_4$Fe(111)* is already more stable than any oxygen adsorbed on Ni$_4$Fe(111) alloy structure. (FeO)$_4$/Ni$_4$Fe(111)* and (FeO)$_6$/Ni$_4$Fe(111)* were additionally constructed. The reason behind the increase of the size of the nanowire is to look not only at the “flat” single layer nanowires (FeO)$_{2\text{-}4}$ but few layers thick (FeO)$_6$ as well, so that different parts of the particle could be analyzed.

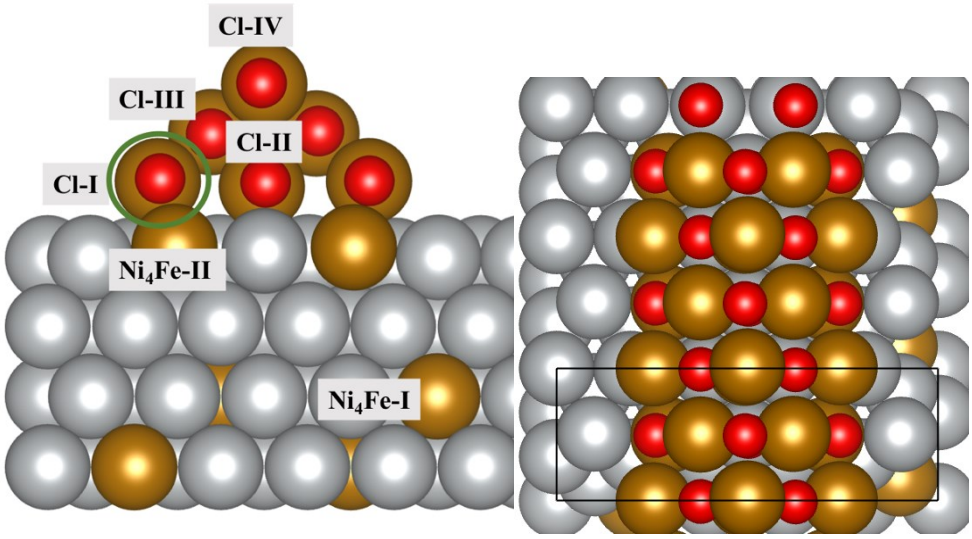

Figure S 25: (FeO)$_6$/Ni$_4$Fe(111)* surface model, side and top view.

(FeO)$_6$/Ni$_4$Fe(111)* model is shown in Figure S 25. Few types of Fe species are present and their Bader Charges are given in Table S 11.

Table S 11: Bader charge of different Fe species in (FeO)$_6$/Ni$_4$Fe* surface model.

Bader charge	Ni$_4$Fe-I	Ni$_4$Fe-II	Cl-I	Cl-II	Cl-III	Cl-IV	FeO

$(FeO)_6/Ni_4Fe(111)$	7.41	7.2	6.87	6.78	6.57	6.6	6.61

Table S10 shows a Bader charge analysis of the Fe in the various structures. Ni_4Fe-I denotes bulk Fe, whereas Ni_4Fe-II denotes Fe located at the surface of the $Ni_4Fe(111)$* alloy. Figure S 26 shows the location of the other Fe atoms at the FeO clusters.

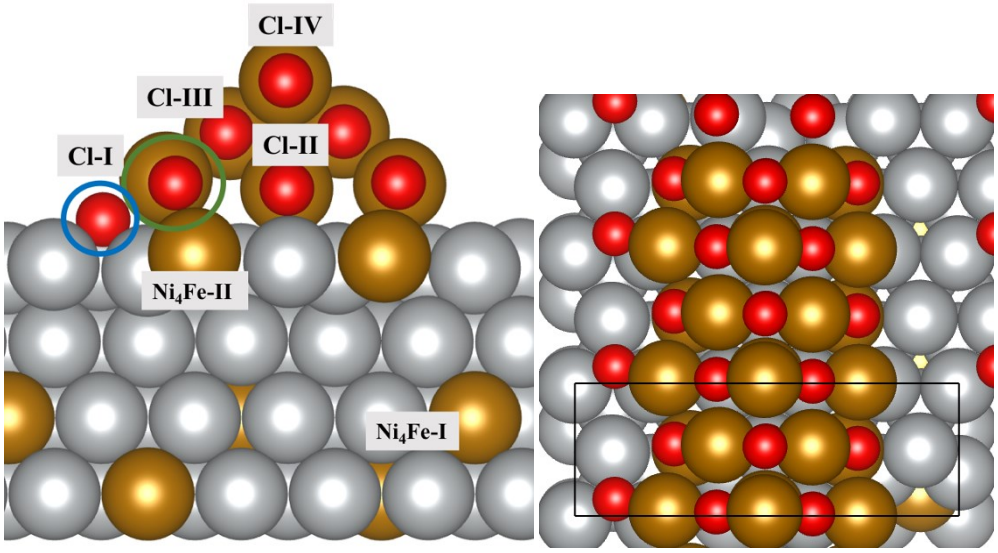

Figure S 26: $O+(FeO)_6/Ni_4Fe(111)$* surface model, side and top view.

Table S 12 shows the Bader charge analysis of a structure with an additional oxygen at the perimeter between FeO and the NiFe alloys.

Table S 12: Bader charge of different Fe species in $O+(FeO)_6/Ni_4Fe$* surface model.

Bader charge	Ni_4Fe-I	Ni_4Fe-II	Cl-I	Cl-II	Cl-III	Cl-IV	FeO
$O+(FeO)_6/Ni_4Fe(111)$	7.41	7.2	6.64	6.78	6.56	6.61	6.61

3.5.5 Phase diagram

For the construction of the final phase diagram, we have used all structures given in Section 3.5.2 and 3.5.3 of SI and we have calculated oxygen binding energies in following way:

For oxygen rich surface alloys:

$xO/Ni_4Fe(111)$ = E(2O/Ni4Fe(111))-E(Ni4Fe(111)-x*μO

for x= 2,3,4

For nanowires:

$(FeO)_y/Ni_4Fe(111)^* = E((FeO)_y/Ni_4Fe(111)^*)-E(Ni_4Fe(111))-2*E(Ni_{bulk})-(y-2)*(Fe_{bulk})-y*\mu O$

$O+(FeO)_6/Ni_4Fe(111)^* = E((FeO)_6/Ni_4Fe(111)^*)-E(Ni_4Fe(111))-2*E(Ni_{bulk})-4*(Fe_{bulk})-7*\mu O$

For y= 2, 3, 4, 6

$\mu O = \mu H_2O-\mu H_2$ – Figure 8 in the main text.

$\mu O = \mu CO_2-\mu CO$ – Figure S 27.

Number of (Fe_{bulk}) is y-2 because $Ni_4Fe(111)^*$ and $Ni_4Fe(111)$ differ in two sublayer Fe atoms.

Number of $E(Ni_{bulk})$ is 2 because $Ni_4Fe(111)^*$ and $Ni_4Fe(111)$ differ in two sublayer Ni atoms.

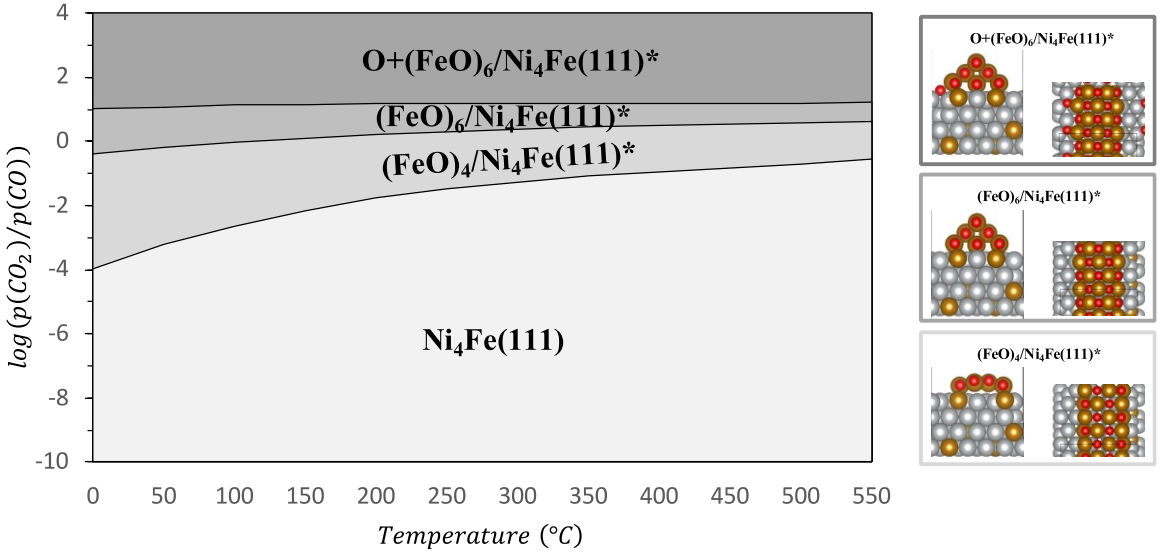

Figure S 27: Phase diagram of $Ni_4Fe(111)$ and $(FeO)_x/Ni_4Fe(111)^*$ system as a function of the pCO_2 / CO ratio and for temperature range between 0 and 550 °C.

3.5.6 Oxygen hydrogenation

To compare the activity of the additional oxygen at the interface O+$(FeO)_6$/Ni4Fe(111)* we calculate the hydrogenation of this oxygen to form H_2O. The results are given in Table S 13: Energy of the first and second hydrogenation steps of interface oxygen and stoichiometric oxygen.

Table S 13: Energy of the first and second hydrogenation steps of interface oxygen and stoichiometric oxygen.

eV	First hydrogenation	Second hydrogenation
O+$(FeO)_6$/Ni_4Fe(111)*	-0.34	-0.35
$(FeO)_6$/Ni_4Fe(111)*	-0.27	+0.33

*3.5.7 Ni vs Ni_4Fe vs $(FeO)_6$/Ni4Fe**

Binding energies of some important intermediates at Ni(111), Ni_4Fe(111) and $(FeO)_6$/Ni_4Fe(111)* surfaces are given in Table S 14 the structures are shown in Figure S 28.

Table S 14: Binding energies of O, CO+O, CO_3 and HCOO at Ni(111), Ni_4Fe(111) and $(FeO)_6$/Ni_4Fe(111)*.

eV	O	CO+O	CO_3	HCOO
Ni(111)	**0.47**	**-0.52**	**0.78**	**-0.87**
Ni_4Fe(111)	0.16	-0.94	0.25	-1.27
$(FeO)_6$/Ni_4Fe(111)*	0.15	-1.02	-0.08	-1.12

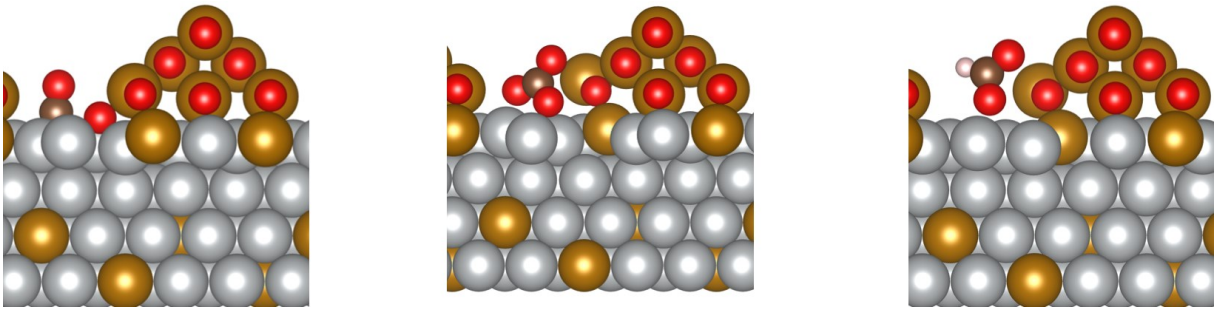

Figure S 28: CO+O, CO_3 and HCOO binding geometries at $(FeO)_x/Ni_4Fe(111)$*.

4 References

[1] J. Rodríguez-Carvajal, *Physica B Condens. Matter* **1993**, *192*, 55-69.

[2] L. Vegard, *Z. Angew. Phys.* **1921**, *5*, 17-26.

[3] Z. Ahmed, J. C. Bevan, *Mineral. Mag.* **1981**, *44*, 225–230.

[4] S. Azadehranjbar, F. Karimzadeh, M. H. Enayati, *Int. J. Mod. Phys B* **2011**, *25*, 1013–1019.

[5] K. H. J. Buschow, P. G. van Engen, R. Jongebreur, *J. Magn. Magn. Mater.* **1983**, *38*, 1–22.

[6] A. Lutts, P. M. Gielen, *Phys. Status Solidi B* **1970**, *41*, K81–K84.

[7] E. A. Owen, E. L. Yates, *Proc. Phys. Soc.* **1937**, *49*, 17–28.

[8] Y. Tanaka, S. Ishida, S. Asano, *Mater. Trans.* **2005**, *46*, 355–360.

[9] R. J. Wakelin, E. L. Yates, *Proc. Phys. Soc. B* **1953**, *66*, 221–240.

[10] H. Zhao, Q. Zhu, Y. Gao, P. Zhai, D. Ma, *Appl. Catal., A* **2013**, *456*, 233–239.

[11] B. Mutz, M. Belimov, W. Wang, P. Sprenger, M.-A. Serrer, D. Wang, P. Pfeifer, W. Kleist, J.-D. Grunwaldt, *ACS Catal.* **2017**, *7*, 6802-6814.

[12] T. Burger, F. Koschany, O. Thomys, K. Köhler, O. Hinrichsen, *Appl. Catal., A* **2018**, *558*, 44-54.

[13] C. Mebrahtu, S. Abate, S. Chen, A. F. Sierra Salazar, S. Perathoner, F. Krebs, R. Palkovits, G. Centi, *Energy Technol.* **2018**, *6*, 1196-1207.

[14] J. Ren, X. Qin, J.-Z. Yang, Z.-F. Qin, H.-L. Guo, J.-Y. Lin, Z. Li, *Fuel Process. Technol.* **2015**, *137*, 204-211.

[15] D. Pandey, G. Deo, *J. Mol. Catal. A: Chem.* **2014**, *382*, 23-30.

[16] H. C. Wu, Y. C. Chang, J. H. Wu, J. H. Lin, I. K. Lin, C. S. Chen, *Catal. Sci. Technol.* **2015**, *5*, 4154-4163.

[17] *NIST Chemistry WebBook*, (available at https://webbook.nist.gov/, accessed on 01.06.2020).